Environmental Research 230 (2023) 115046

Contents lists available at ScienceDirect

Environmental Research

journal homepage: www.elsevier.com/locate/envres

Cytotoxicity of fibrous antigorite from New Caledonia

Elena Gazzano [a,d,1], Jasmine Rita Petriglieri [b,d,1], Elisabetta Aldieri [c,d], Bice Fubini [b,d], Christine Laporte-Magoni [e], Cristina Pavan [b,d], Maura Tomatis [b,d,*], Francesco Turci [b,d]

[a] Department of Life Sciences and Systems Biology, University of Torino, Via Accademia Albertina 13, 10123, Torino, Italy
[b] Department of Chemistry, University of Torino, V. P. Giuria 7, 10125, Torino, Italy
[c] Department of Oncology, University of Torino, V. Santena 5 bis, 10126, Torino, Italy
[d] "G. Scansetti" Interdepartmental Center for Studies on Asbestos and Other Toxic Particulates, University of Torino, Torino, Italy
[e] Institute of Exact and Applied Sciences, University of New Caledonia, BPR4, Nouméa, France

ARTICLE INFO

Keywords:
Fibrous antigorite
Surface reactivity
Chemical alteration
Cellular toxicity
Oxidative stress
Inflammation

ABSTRACT

Exposure to asbestos and asbestos-like minerals has been related to the development of severe lung diseases, including cancer and malignant mesothelioma (MM). A high incidence of non-occupational MM was observed in New Caledonia (France) in people living in proximity of serpentinite outcrops, containing chrysotile and fibrous antigorite. Antigorite is a magnesium silicate, which shares with chrysotile asbestos the chemical formula. To achieve information on antigorite toxicity, we investigated the physico-minero-chemical features relevant for toxicity and cellular effects elicited on murine macrophages (MH-S) and alveolar epithelial cells (A549) of three fibrous antigorites (f-Atg) collected in a Caledonian nickel lateritic ore and subjected to supergene alteration. Field Atg were milled to obtain samples suitable for toxicological studies with a similar particle size distribution. UICC chrysotile (Ctl) and a non-fibrous antigorite (nf-Atg) were used as reference minerals.

A high variability in toxicity was observed depending on shape, chemical alteration, and surface reactivity. The antigorites shared with Ctl a similar surface area (16.3, 12.1, 20.3, 13.4, and 15.6 m^2/g for f-Atg1, 2, 3, nf-Atg, and Ctl). f-Atg showed different level of pedogenetic weathering (Ni depletion f-Atg1 $\ll$ f-Atg2 and 3) and contained about 50% of elongated mineral particles, some of which exhibited high aspect ratios (AR $>$ 10 μm, 20%, 26%, 31% for f-Atg1, 2, and 3, respectively). The minerals differed in bio-accessible iron at pH 4.5 (f-Atg1 $\ll$ f-Atg3, $<$ f-Atg2, nf-Atg $<$ Ctl), and surface reactivity (ROS release in solution, f-Atg1 $\ll$ f-Atg2, 3, nf-Atg, and Ctl). f-Atg2 and f-Atg3 induced oxidative stress and pro-inflammatory responses, while the less altered, poorly reactive sample (f-Atg1) induced negligible effects, as well nf-Atg. The slow dissolution kinetics observed in simulated body fluids may signal a high biopersistence. Overall, our work revealed a significative cellular toxicity of f-Atg that correlates with fibrous habit and surface reactivity.

1. Introduction

The term asbestos applies to six fibrous minerals of the amphibole (crocidolite, amosite, actinolite, anthophyllite, and tremolite) and serpentine group (chrysotile) used in the past for a variety of industrial applications. Inhalation of asbestos fibers causes severe lung diseases, such as mesothelioma and lung cancer (IARC, 2012). Asbestos ban has significantly reduced health risk. However, cases of mesothelioma are still observed in many countries as a consequence of para-occupational or environmental exposure. Pleural mesothelioma has been described also in individuals exposed to fibrous minerals with asbestos-like structure and morphology that occur naturally in rocks and soils, such as erionite in Turkey (Carbone et al., 2011), fluoro-edenite in Italy (Gianfagna et al., 2003), and winchite/richterite in the United States (EPA, 2014; Whitehouse et al., 2008). In New Caledonia (NC) a high incidence of mesothelioma was observed in people living in proximity of serpentinite outcrops, containing chrysotile and fibrous antigorite (Baumann et al., 2011). Due to the widely serpentine distribution over a large part of the Caledonian island (more than a third of the land) and by adopting a precautionary principle, the Government of New Caledonia classified antigorite, without distinction between fibrous and non-fibrous form, as regulated asbestos (Délibération N°82 du 25 aout

* Corresponding author. Department of Veterinary Sciences, University of Torino, Largo Braccini, 2, 10095, Grugliasco, TO, Italy.
E-mail address: m.tomatis@unito.it (M. Tomatis).
[1] These authors equally contributed.

https://doi.org/10.1016/j.envres.2022.115046
Received 30 August 2022; Accepted 9 December 2022
Available online 12 December 2022

2010). Antigorite is a member of the serpentine group, that shares chemical composition with chrysotile asbestos (ideal chemical formula: $Mg_3Si_2O_5(OH)_4$). Antigorite may exhibit lamellar or fibrous shape (Baur, 2018). The lamellar form is the most widespread form of antigorite, but fibrous antigorite has been recently found, besides in New Caledonia, in Western Alps (Europe) (Belluso et al., 2020; Vortisch and Baur, 2018), and southern Australia (Baur, 2018). Distinction between chrysotile and fibrous antigorite is sometimes difficult by use of standard procedure for asbestos analysis (e.g., SEM-EDS).

Unlike chrysotile, antigorite has not been exploited for commercial purposes and has received little attention in the past from a toxicological point of view, as people were not expected to be exposed. Few experimental studies are currently available. Fibrous antigorite showed dose-dependent cytotoxicity, stimulated reactive oxygen species (ROS), nitric oxide (NO), and prostaglandin E2 generation in mesothelial and macrophage cells (Cardile et al., 2007), and induced production of effector molecules influencing neoplastic cell growth (Vascular Endothelial Growth factor-VEGF-, cell division control protein 42 -Cdc 42-and β-catenin) in lung epithelial cells (Pugnaloni et al., 2010). As opposed to the fibrous form, lamellar antigorite did not elicit cytotoxic effect (Mossman and Sesko, 1990) and did not increase cell proliferation (Marsh and Mossman, 1988; Sesko and Mossman, 1989; Woodworth et al., 1983). Only two studies have investigated the in vivo effect of antigorite. These studies date back to the 1980s–90s and evidenced fibrogenic (increase of hydroxyproline lung content) (Wozniak, 1984) and carcinogenic (peritoneum mesothelioma development) (Wozniak et al., 1993) activity of dust containing fibrous antigorite in rats.

The interest in antigorite toxicity recently increased (ANSES, 2014; Baur, 2018; FitzGerald et al., 2010; Petriglieri et al., 2021; Petriglieri et al., 2020); as a consequence of the finding of the cases of mesothelioma in NC and the increased awareness about the risk due to environmental exposure to asbestos (Harper, 2008) and non-regulated potentially hazardous fibrous minerals.

The purpose of the present study is to investigate antigorite toxicity by using a set of physico-chemical and cellular assays aimed to evaluate which of the features implied in asbestos toxicity are present in antigorite.

Even if the mechanism is not still fully clarified, the scientific community recognizes i) size and shape, ii) biopersistence and iii) surface reactivity of fibers as key modulators of asbestos toxicity (IARC, 2012; Turci et al., 2017).

Size affects the fate of fibers into the lung (penetration, deposition, translocation, and clearance): only fibers with width <3 μm penetrate the lung and reach the alveoli, where they can accumulate or be cleared by alveolar macrophages. Macrophage clearance depends upon fiber length. Fibers shorter than 5 μm are completely phagocytized, whereas long fibers cannot be fully engulfed and may lead to frustrated phagocytosis. Thin and long fibers may easily translocate to the pleura and, consequently, are the most potent in driving mesothelioma development (Stanton et al., 1981).

Biopersistence refers to the extent to which a fiber "is able to resist chemical, physical and other physiological clearance mechanisms in the body" (Utembe et al., 2015) and strongly depends on fiber solubility. Clearly, longer the biopersistence, higher the potential toxic effects.

The surface reactivity here refers to the potency of a mineral surface to react with biomolecules. Iron-mediated reactivity of asbestos in free radical generation is well demonstrated (Gualtieri et al., 2019; Kamp and Weitzman, 1999). Generation of oxidant species, both directly by fibers and indirectly by cells after fiber phagocytosis, is responsible for the onset of oxidative stress and contributes to the induction of an inflammatory response that, if persistent, leads to fibrosis and cancer (IARC, 2012).

On the basis of the knowledge acquired on asbestos toxicity, a set of three fibrous antigorite samples was examined for a) shape and fiber size distribution, b) solubility in simulated body fluids, c) surface reactivity (e.g., presence of bioavailable iron, ability to catalyze free radical generation and to deplete antioxidant molecules). In addition, cytotoxicity, ability to induce oxidative stress and pro-inflammatory response were investigated on murine alveolar macrophages (MH-S) and human alveolar epithelial cells (A549). The three samples were collected in a nickel open pit mine in NC and are representative of fibrous antigorite in NC lateritic Ni ores. Nickel laterite ores are the product of supergene alteration of ultramafic rocks under humid sub-tropical conditions. Supergene processes occurred at the upper horizons of the lateritic profile and include meteoric water circulation, which promotes leaching and redistribution of the elements, and consequent chemical alteration of the minerals. The three selected samples differ for chemical alteration, from Ni-enriched and less-altered to Ni- and Mg-depleted and more altered samples, and for macroscopically cohesion state, from massive to weakly cohesive (Petriglieri et al., 2021). A non-fibrous antigorite was also used to assess the role of fibrosity in cellular responses.

2. Materials and methods

2.1. Antigorite

Fibrous antigorite specimens were from Tontouta mine (NC) and are thoroughly described in previous work (Petriglieri et al., 2021). The three samples differ for i) cohesion, from massive (f-Atg1) to moderately (f-Atg2) to weakly cohesive (f-Atg3); and ii) chemical alteration, from Ni-enriched and less-altered (f-Atg1) to Ni- and Mg-depleted and more altered (f-Atg2 and f-Atg3). Samples f-Atg1, 2, and 3 were samples T1, T3 and T7 in Petriglieri et al. (2021). Non-fibrous Atg (nf-Atg) was from Val di Susa (Italy; Groppo et al., 2006). Their composition is reported in Table 1. UICC chrysotile A from Zimbabwe (Ctl) was used as a reference sample. Man-Made Mineral Fibers (MMVF 10 glass fibers) were used as negative control in cellular tests. NC antigorites were gently crushed in a ball mixer mill for 2–5 min at 27 Hz in agate jars to obtain samples with similar content of fibers, suitable for toxicological studies.

2.2. Physico-chemical features

2.2.1. Surface area

The surface area was measured by means of the BET method based on Kr adsorption at 77 K (ASAP 2020 Micrometrics, Norcross, GA). All samples were outgassed at 150 °C for 2 h prior the analysis.

2.2.2. Chemical analysis

Mineral chemistry analysis was performed on petrographic thin sections with a Scanning Electron Microscope associated to Energy dispersive X-ray spectroscopy (SEM-EDS) JEOL JSM IT 300 LV equipped with an Oxford INCA Energy 200 ED. Microanalysis operating conditions were 15 kV and 5 nA, 10^5 CPS and 30 s counting time; relative wt. % errors are <1% for major elements and <5% for minor components. Standards comprise pure elements, simple oxides or simple silicate compositions. Before the analysis, samples were coated with a carbon layer. Statistical data treatment was performed with OriginPro® software. The full set chemical analysis of NC antigorite samples is reported in (Petriglieri et al., 2021).

2.2.3. Mineral identification

Mineral identification was confirmed by micro-Raman spectroscopy. Raman spectra were obtained with a Horiba JobinYvon HR800 Raman spectrometer equipped with an Olympus BX41 confocal microscope, a 600-grooves/mm holographic grating monochromator and a high-gain Peltier-cooled CCD. A Nd solid state laser at 532-nm has been used as excitation and density filters were used to avoid sample heating. Spectra were obtained on 50 (elongated) particles with a 100x objectives. Under these working conditions, the minimum lateral resolution is around 2 μm. The spectrometer calibration was carried out using the 520.7 cm^{-1} Raman peak of silicon before each experimental session. Spectra were collected for 1 min (6 acquisitions for 10s) in the low and high

wavenumber spectral range. Data treatment was performed with LabSpec® software.

2.3. Morphology and size distribution

Particle morphology was evaluated by a FE-SEM TESCAN S9000G equipped with a Schottky FEG source. Antigorite was deposited on a graphite tape and covered with a 4 nm thick Au layer. Electron images were acquired at various magnifications (100–2000x) and accelerating voltages (3–10 kV).

Particle size distribution was obtained by automated flow particle image analysis using the Sysmex FPIA-3000 apparatus (Malvern Instruments, U.K., detection range 0.8–160 μm). Antigorite was dispersed in ultrapure water (0.5 mg/ml) and sonicated for 30 s at 10 W. Each suspension was passed through a cell where images of particles were captured using stroboscopic illumination and a CCD camera. Each sample was run at least four times with objective lens at 20x magnification in both High and Low Power Field mode. The four analyses were then pooled to obtain a statistically sound size distribution. About 7500 particles were analyzed for each sample.

Fibers size distribution of the respirable fraction (AR $\geq$3, L $>$ 5 μm, W $<$ 3 μm) was evaluated by SEM. SEM Images were acquired at 2500x and 10 kV. About 300 fibers were measured for each f-Atg specimen.

2.4. Dissolution in simulated body fluids

The dissolution was analyzed under static condition. Samples (1 mg/ml) were incubated in phagolysosomal simulant fluid (PSF) (Stefaniak et al., 2005) and Gamble's solution (Scholze and Conradt, 1987), and kept in the dark at 37° for 28 days under gently shaking. Supernatants obtained by filtration on cellulose acetate filter membranes (porosity 0.45 μm) were processed by ICP-AES (IRIS II Advantage/1000 Radial Plasma Spectrometer, Thermo-Jarrell Ash Corp.) to quantify Mg and Si leaching.

2.5. Surface reactivity

2.5.1. Determination of bioavailable iron

The samples were incubated (1 mg/ml) in 1 mM ferrozine or 1 mM ferrozine and 1 mM of ascorbic acid to evaluate bioavailable Fe^{2+} and total bioavailable iron (Fe^{2+} + Fe^{3+}), respectively. The amount of iron extracted was quantified spectrophotometrically (Uvikon 930-Kontron Instrument) on the supernatant by measuring the absorption of the iron-ferrozine complex at 562 nm.

2.5.2. Free radical generation

Particle-free radical release was evaluated in cell free tests by means of spin trapping technique associated with EPR spectroscopy. EPR spectra were recorded on Miniscope MS 100 (Magnettech, Berlin, Germany) spectrometer. The instrument settings were as follows: microwave power 10 mW; modulation 1000 mG; scan range 120 G; center of field 3345 G. The number of radicals released is proportional to the intensity of the EPR signal. The signals were double integrated and numeric values were reported as arbitrary units, in order to compare the production of free radicals by the different samples. Blanks were performed in parallel in the absence of sample. All the experiments were repeated at least twice.

- Generation of $^{\bullet}OH$ radicals was measured by suspending 25 mg of fibers in 500 μL of 1 M phosphate buffered solution (pH 7.4), then adding 250 μL of 0.17 M DMPO (the spin trap agent) and 250 μL of 0.20 M H_2O_2 as target molecule. The radical formation was evaluated by recording the EPR spectrum of the [DMPO-OH]$^{\bullet}$ adduct at 10, 30, and 60 min.
- Generation of $^{\bullet}CO_2^-$ radicals was measured both in presence and absence of ascorbic acid (AA) by suspending 25 mg of fibers in 250 μL of 0.17 M DMPO, then adding 250 μL of 6 mM AA or 250 μL of MilliQ water and 500 μL of 2 M of sodium formate, as target molecule, in phosphate buffer 1 M. The radical formation was evaluated by recording the EPR spectrum of the [DMPO-CO_2^-]$^{\bullet}$ adduct at 10, 30, and 60 min. AA was used to reduce Fe^{3+} to Fe^{2+} and activate oxidized surfaces.

2.5.3. Ascorbic acid and glutathione depletion

Suspensions (1.0 mg/ml) were prepared in a 0.1 mM solution of ascorbic acid (AA) or glutathione (GSH) in phosphate buffer (0.01 M, pH 7.4). The suspensions were stirred at 37 °C for 5 h. At regular time intervals, the suspensions were centrifuged (RCF = 8500 g, 10 min, Rotina 380, Hettich GmbH & Co.). The amount of AA in the supernatant was measured spectrophotometrically (Uvikon 930, Kontron Instrument) at 265 nm. The amount of GSH was measured at 412 nm after reaction with Ellman's reagent. All experiments were performed in duplicate. The results are expressed per unit surface area and reported as average values ± standard deviation.

2.6. Cellular tests

2.6.1. Cell culture preparation

Human lung epithelial cells (A549) were obtained by American Type Culture Collection (ATCC) and murine alveolar macrophages (MH-S) were provided by Istituto Zooprofilattico Sperimentale "Bruno Ubertini" (Brescia, Italy). Cells were cultured in 35- (1.2×10^6 cells) or 100-mm-diameter petri dishes (7.5×10^6 cells) in RPMI-1640 medium (Invitrogen Life Technologies, CA, USA) supplemented with 10% fetal bovine serum (FBS) and 1% penicillin/streptomycin, up to confluence, and then incubated for 24 h in the presence of different amount of antigorite samples (15–120 μg/ml) or with 30 μg/ml UICC chrysotile asbestos, used as a positive control, and MMVF10 fibers (120 μg/ml) used as negative control. All samples were sonicated (100 W: 30 s; Labsonic Sonicator; Sartorius Stedim Biotech S.A., Aubagne, France) before incubation with cell cultures to allow better suspension in the culture medium.

The protein content of the monolayers and cell lysates was assessed with the BCA kit from Sigma-Aldrich (St Louis, MO, USA). Plastic ware was purchased from Falcon (Becton Dickinson, Franklin Lakes, NJ). Unless otherwise specified, other reagents were purchased from Sigma-Aldrich.

2.6.2. Cytotoxicity assay - lactate dehydrogenase (LDH) leakage

Cytotoxic activity was assessed by investigating cell membrane integrity after 24 h of sample exposure by measuring the leakage of LDH activity into the extracellular medium at a wavelength of 340 nm (37 °C) with a microplate reader (Benchmark Plus, Bio-Rad). The procedure described in Polimeni et al. (2008) was followed. Both intracellular and extracellular enzyme activity was expressed as μmol of NADH oxidized/min/dish, then extracellular LDH activity (LDH out) was calculated as a percentage of the total LDH activity (LDH tot = intracellular + extracellular) in the dish.

2.6.3. Oxidative stress

2.6.3.1. ROS generation. ROS generation was detected by loading A549 cells and MH-S for 30 min with 10 μM 2′,7′-dichlorodihydrofluorescein diacetate (DCFH-DA) after a 24 h incubation in the absence or presence of 15, 30, 60, and 120 μg/ml of antigorite, 30 μg/ml chrysotile, or 120 μg/ml MMVF10. DCFH-DA is a cell-permeable probe that is cleaved intracellularly by (non-specific) esterases to form DCFH, which is further oxidized by ROS to form the fluorescent compound dichlorofluorescein (DCF). The cells were washed twice with PBS and the DCF fluorescence was determined at an excitation wavelength of 504 nm and emission wavelength of 529 nm, using a Synergy HT microplate reader (Bio-Tek

Instruments, Winooski, VT, USA). The fluorescence value was expressed as arbitrary fluorescence unit (a.u.f.).

2.6.3.2. Measurement of enzyme activity. Glucose 6-phosphate dehydrogenase (G6PD) and 6-phosphogluconate dehydrogenase (6 PGD) activities were measured after 24 h of incubation with 120 μg/ml antigorite or 30 μg/ml chrysotile or 120 μg/ml MMVF10. Cells were washed with fresh medium, detached with trypsin/EDTA, washed with PBS, resuspended at $0.1 \times 10_6$ cells/ml in 0.1 M Tris/0.5 mM EDTA pH 8, and sonicated on ice with two 10 s bursts. This cell lysate was checked for the activity of G6PD and 6 PGD using a Synergy HT microplate reader, as previously described (Riganti et al., 2002).

2.6.3.3. Heme oxygenase 1 (HO-1) expression. A549 cells after a 24 h incubation with 120 μg/ml antigorite or 30 μg/ml chrysotile or 120 μg/ml MMVF10 were lysed in a buffer (25 mM HEPES, 135 mM NaCl, 1% NP40, 5 mM EDTA, 1 mM EGTA, 1 mM ZnCl2, 50 mM NaF, 10% glycerol) supplemented with a protease inhibitor cocktail set III (100 mM AEBSF, 80 μM aprotinin, 5 mM bestatin, 1.5 mM E−64, 2 mM leupeptin, and 1 mM pepstatin; Calbiochem-Novabiochem Corporation, San Diego, CA), 2 mM phenylmethylsulfonyl fluoride, and 1 mM sodium orthovanadate. HO-1 protein was separated by sodium dodecyl sulfate polyacrylamide gel electrophoresis (SDS-PAGE; 12%), transferred to a polyvinylidene difluoride (PVDF) membrane sheet, and probed with the rabbit anti–HO–1 antibody (D.B.A. Italia s. r.l., Milan, Italy), diluted 1:1000 in PBS–bovine serum albumin (BSA) 1%, and/or anti-GAPDH (Santa Cruz Biotechnology, Santa Cruz, CA), diluted 1:500 in PBS–BSA 1%. After overnight incubation, the membrane was washed with PBS-Tween 0.1% and was subjected for 1 h to a peroxidase-conjugated anti-rabbit immunoglobulin (Ig) G (sheep, Amersham International, Bucks, UK; diluted 1:1000 in PBS-Tween with blocker nonfat dry milk 5%, Bio-Rad Laboratories, CA, USA). The membrane was washed again with PBS-Tween 0.1% and proteins were detected by enhanced chemiluminescence (PerkinElmer, Shelton, CT).

2.6.3.4. Measurement of intracellular glutathione. Reduced glutathione (GSH) was measured as described by Vandeputte et al. (1994), using a glutathione reductase-Ellman reagent recycling assay and Synergy HT microplate reader. Intracellular levels of GSH were measured after a 24 h incubation with 120 μg/ml antigorite or 30 μg/ml chrysotile or 120 μg/ml MMVF10.

2.6.4. Oxidative damage

2.6.4.1. Measurement of malonyldialdehyde (MDA). After a 24 h incubation with 120 μg/ml antigorite or 30 μg/ml chrysotile or 120 μg/ml MMVF10, cells were washed with fresh medium, detached with trypsin/EDTA, and resuspended in 1 ml of PBS. Lipid peroxidation was spectrophotometrically detected with a Synergy HT microplate reader measuring the intracellular level of MDA, the end product derived from the breakdown of polyunsaturated fatty acids and related esters, with the lipid peroxidation assay kit (Oxford Biomedical Research, Oxford, MI), which uses the reaction of N-methyl-2-phenylindole with MDA in the presence of hydrochloric acid to yield a stable chromophore with maximal absorbance at 586 nm (Gerard-Monnier et al., 1998).

2.6.4.2. Alkaline comet assay. Single-cell gel electrophoresis (comet assay) was performed under alkaline conditions according to the method of Singh and colleagues (Singh et al., 1988) with slight modifications. All steps were conducted under dim yellow light to prevent additional DNA damage. After a 24 h incubation with 60 μg/ml antigorite or 30 μg/ml chrysotile or 120 μg/ml MMVF10, 7.5 μL A549 suspension (5×10^4 cells) was mixed with 75 μL low melting point agarose (0.8%) and placed on the clear part of a frosted microscope slide precoated with a layer of normal melt point agarose (1%) and low melting point agarose. Then, slides were immersed in lysis buffer for 1 h (4 °C, 2.5 M NaCl, 0.1 M Na_2EDTA, 10 mM Tris, 0.5% N-laurylsarcosine, supplemented with 1% Triton X-100 just before use). To perform the DNA unwinding, slides were placed in a horizontal electrophoresis unit containing the electrophoresis buffer (300 mM NaOH, 1 mM Na_2EDTA, pH > 13) for 40 min. Alkaline electrophoresis was performed in the same buffer for 20 min (25 V, 300 mA). Slides were washed three times with neutralization buffer (0.4 M Tris, pH 7.5) and then they were dehydrated in 70% ethanol (5 min) and left to dry, allowing the storage until analysis. To analyse DNA damage, slides were stained with DAPI (10 μg/ml, 5 min). Fifty randomly chosen, non-overlapping comets per comet slide were observed using a Leica fluorescence microscope (20X objective) and an image analysis system (CometScore, TriTek Corp. USA).

2.6.5. Pro-inflammatory response

2.6.5.1. Nitric oxide (NO) synthesis. After a 24 h incubation with control and 15, 30, 60, and 120 μg/ml of antigorite, 30 μg/ml chrysotile, or 120 μg/ml MMVF10, the extracellular medium was collected and the concentration of nitrite (the stable product of NO synthesis) was measured with the Griess method (Ghigo et al., 1998). Nitrite was measured at 540 nm with a Synergy HT microplate reader. A blank was prepared in the absence of cells and its absorbance was subtracted from the one measured in the samples; absorbance values were also corrected for the monolayer proteins and results were expressed as nmol/mg cellular protein.

2.6.5.2. Measurement of tumor necrosis factor-α (TNF-α). After a 24 h incubation with 120 μg/ml of antigorite, 30 μg/ml chrysotile, or 120 μg/ml MMVF10, the extracellular medium was collected and centrifuged at 13000 g for 30 min. The concentration of each cytokine in the supernatant was determined by using the Conventional ELISA kits from Bender MedSystems (Vienna, Austria), following the manufacturer's instructions. The absorbance was measured at 450 nm with a Synergy HT microplate reader. The cytokines amount was corrected for the content of cell proteins, and the results were expressed as pg/mL/mg cellular protein.

3. Results and discussion

3.1. Physico-chemical features of the three fibrous antigorites

3.1.1. Chemical composition

Chemical composition of each sample is reported in Fig. 1. Mg content in antigorite (Atg) was, as expected, lower than in chrysotile (Ctl). Both minerals, indeed, consist of octahedral layers [O] rich in Mg (brucite sheet) attached to SiO_4 tetrahedral layers [T], but differ in their spatial arrangement. Ctl exhibits tubular shape with an external, easily accessible brucite layer, whereas Atg possesses a modulated structure (Wicks and O'Hanley, 1988) with the periodic inversion of [T] with respect to [O] layer. This results in a significant omission of octahedral sites in Atg with a loss of Mg with respect to Si (Deer et al., 2009; Wicks and Whittaker, 1975).

Iron amount ranged between 2 and 3 wt% and did not significantly differ among samples. Specimens f-Atg2 and f-Atg3 were Mg-rich and Ni-poor, while f-Atg1 shows a low Mg + Fe content and a relative high Ni content. These compositional differences are highlighted in the ternary diagrams (Fig. 1 and Fig. S1) and are a consequence of the different degree of supergene alteration that weathered the Atg minerals to different extent, namely f-Atg1 < f-Atg2 ≈ f-Atg3.

Contamination with chrysotile was investigated by micro-Raman spectroscopy. Raman analysis revealed no (f-Atg1) or negligible (1 Ctl fiber out of 50 fibers of f-Atg2 and f-Atg3 analyzed) contamination (data not shown) and Atg samples could be reasonably considered as "pure phases". Mineralogical purity is an element of particular importance in

	f-Atg1	f-Atg2	f-Atg3	nf-Atg	Ctl
SiO_2	43.66	44.19	44.13	42.72	39.90
Al_2O_3	0.25	0.19	0.23	1.83	0.76
Cr_2O_3	0.00	0.00	0.00	0.00	0.23
FeO	2.34	1.95	2.72	2.82	2.26
NiO	2.00	0.53	0.55	0.00	0.21
MgO	37.72	39.30	38.64	39.31	42.60
MnO	0.00	0.11	0.07	0.00	0.06
CaO	0.06	0.00	0.06	0.00	0.33
Tot	*86.14*	*86.42*	*86.67*	*86.96*	*86.35*
Si	2.069	2.068	2.072	2.018	1.867
Al	0.013	0.011	0.013	0.102	0.044
Cr	0.000	0.000	0.000	0.000	0.025
Fe	0.076	0.076	0.107	0.111	0.088
Ni	0.093	0.020	0.022	0.022	0.008
Mg	2.664	2.741	2.703	2.768	2.971
Mn	0.000	0.005	0.002	0.00	0.004
Ca	0.004	0.000	0.004	0.000	0.016

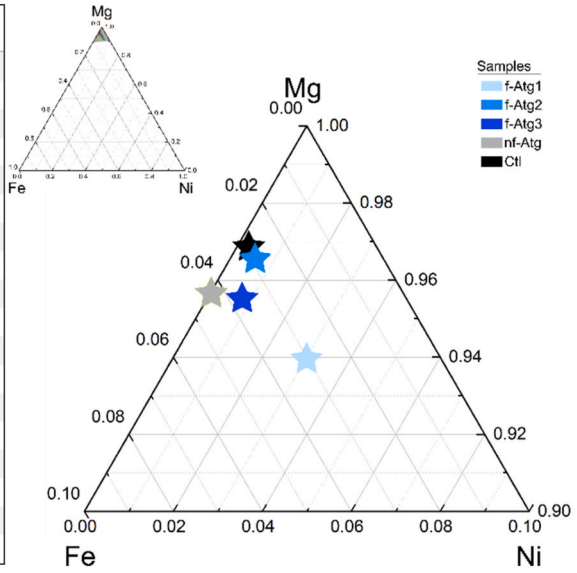

Fig. 1. Chemical composition of the Atg specimens. Representative chemical analyses (in weight percent of oxides) and structural formulae (in atoms per formula unit) of Atg and Ctl (left). Chemical analyses were normalized on the basis of seven oxygen. The full set of EDS analyses is reported in (Petriglieri et al., 2021). Ternary diagram (right) considering Mg, Fe, and Ni elements showing the variability in chemical composition of antigorite samples and Ctl. Specimen f-Atg1 exhibits a high Ni content and a relative low Mg + Fe content. Data were plotted as atoms per formula unit.

toxicological studies on serpentine minerals. In fact, due to the typical closely intergrowth of Atg and Ctl minerals in metamorphic context (Groppo and Compagnoni, 2007; Tarling et al., 2018), the preparation of a pure specimen is often quite challenging.

3.1.2. *Surface area*

Specific surface areas determined using BET (Brunauer–Emmett–Teller) method were: f-Atg1 16.3 m^2/g; f-Atg2 12.1 m^2/g; f-Atg3 20.3 m^2/g; nf-Atg 13.4 m^2/g. BET area of UICC chrysotile A is 15.6 m^2/g.

3.1.3. *Morphology and particle size distribution*

SEM images of pristine Atg (left column) and ground Atg (central and right columns) are reported in Fig. 2. The gentle, sample-specific grinding procedure was aimed at obtaining three Atg specimens with similar amount of elongated particles (EMPs, Aspect Ratio Length/Width $\geq$3). Poly-filamentous bundles of elongated fibro-lamellar crystals with splaying ends and several EMPs separated longitudinally into thinner fibers were observed on pristine Caledonian Atg. After grinding, many particles still exhibited an elongated shape. This suggests that the selected Atg minerals preferentially break along the z-axis, in a similar fashion to asbestos minerals. SEM analysis of the ground material evidenced both "regulated respirable fibers" according to the WHO definition (AR$\geq$3, W < 3 μm, and L > 5 μm) and non-respirable fibers, *i.e.*, elongated particles with lamellar habit and plane-parallel cleavage surfaces that do not origin fibril bundles and usually exhibit diameter ticker than asbestos fibers. Conversely, Atg from Susa Valley (nf-Atg) exhibited elongated but short and thick crystals.

A quantitative analysis of particle size distribution (PSD) of ground Atg specimens was carried out by means of a light microscope enhanced with an automatic image analysis software, which allowed the analysis of a relevant number of particles (about 7′500 particles for each sample). PSD scatter plots, showing the presence of a large part of particles in respirable size, are shown in Fig. S2 (red-shaded box), while the amount of "particles", "respirable fibers", and "non-respirable fibers" is reported in Fig. 3.

After grinding, all fibrous antigorite specimens showed about 50–60% of EMPs. f-Atg1 showed about 17% of long and thick non-respirable fibers and 43% of respirable fibers. f-Atg2 and f-Atg3 contained 35% and 39% of respirable fibers and 12% and 13% of non-respirable fibers, respectively.

As mineral fragments are generally considered non-hazardous in particle toxicology due to their morphology, and non-respirable fibers (W $\geq$ 3 μm) are also considered non-hazardous by inhalation due to their high aerodynamic equivalent diameter, we focused on respirable fibers. Thin and long fibers are historically considered more hazardous than shorter ones (Barlow et al., 2017; Boulanger et al., 2014; Stanton et al., 1981). Epidemiological, experimental, and computational (Berman and Crump, 2008; Korchevskiy and Wylie, 2022; Wylie et al., 1993) studies showed a significant correlation between carcinogenicity and fiber length and width, in particular fibers thinner than 0.4 μm were considered to cause the most damage. To gain insight of these morphological parameters, we characterized the respirable fraction of the ground f-Atg specimens by measuring length and width of ca. 300 fibers per specimen. The scatter plots of AR as a function of fiber width, the relative and cumulative PSD obtained by analyzing width and length by SEM are reported in Fig. 4 (upper to lower panel). Most of the fibers were shorter than 10 μm in length. The most represented length class was between 5 and 10 μm for f-Atg1 and f-Atg2, and between 5 and 8 μm for f-Atg 3. Most of the respirable fibers showed width <1 μm. Fibers with AR > 10 accounted for 47%, 73%, and 80% of the respirable fibers in f-Atg-1, f-Atg-2, and f-Atg3, corresponding to 20, 26 and 31% of the whole sample, respectively. Furthermore, more than 40% of the respirable fibers with AR>10 in f-Atg-2 and f-Atg3 were thinner than 0.4 μm, while long and thin fibers accounted for 9% of the respirable fraction in f-Atg1. The overall high aspect ratios and thin widths exhibited by the three Atg specimens after milling, clearly indicates that these mineral specimens split in an asbestos-like fashion (Berman and Crump, 2003; Harper et al., 2008).

3.2. *Dissolution in simulated body fluids*

Antigorite dissolution was evaluated in two models of biological fluids: a solution simulating phagolysosomal fluid (PSF, pH 4.5) and the Gamble's solution (pH 7.4) which reproduces the composition of bronchoalveolar fluids. Fig. 5 A and B compares the kinetics of Mg and Si release of f-Atg2, chosen as the specimen representative for the Atg samples, and chrysotile in PSF and Gamble's solution, respectively. The amount of Mg and Si leached after 1 month by the other Atg specimens is reported in Fig. S3. Dissolution of both Atg and Ctl proceeded faster at low pH, with preferential release of Mg ions from the octahedral layer.

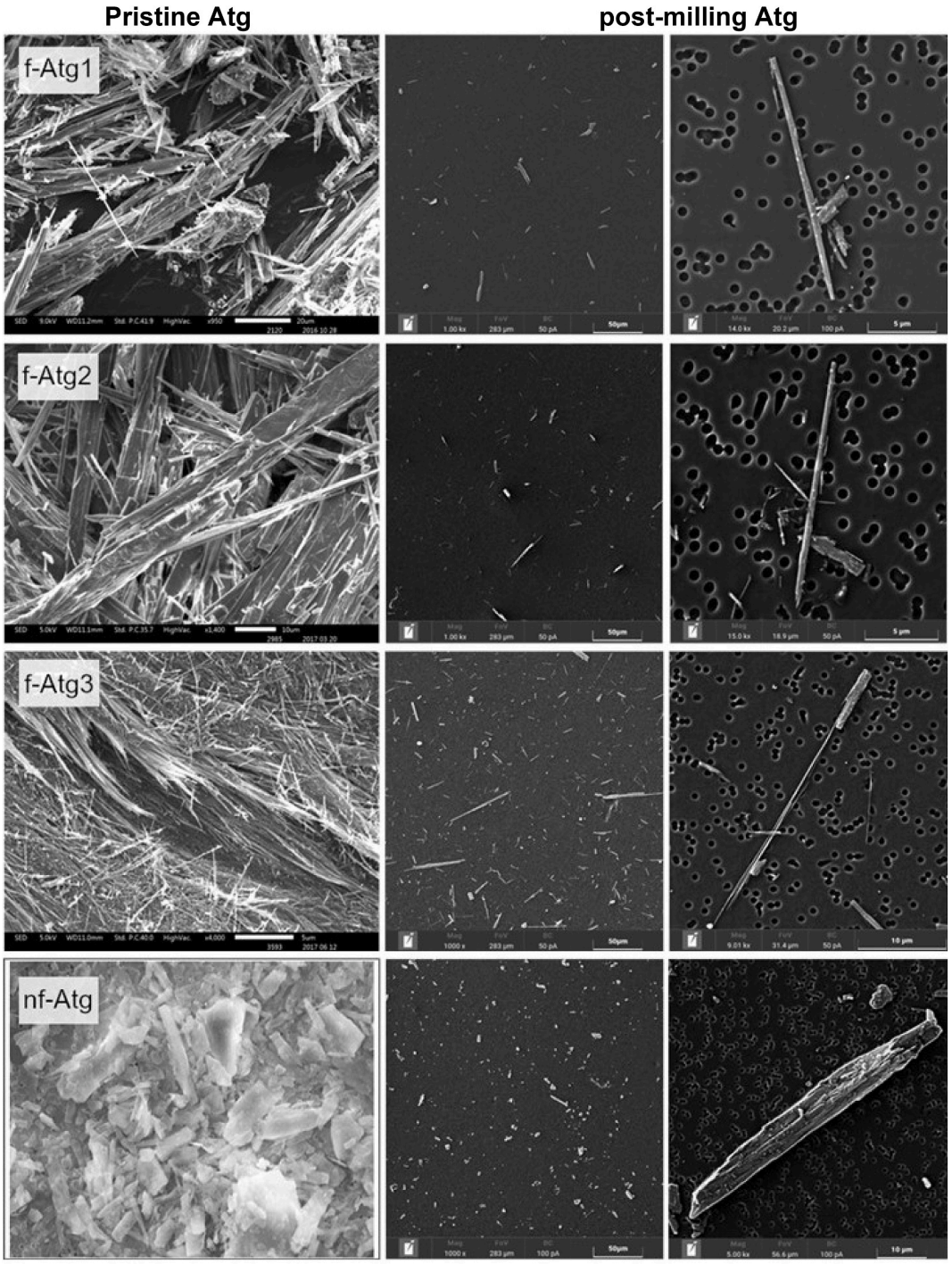

Fig. 2. Antigorite morphology. SEM images of f-Atg1, f-Atg2, f-Atg3 and nf-Atg: pristine samples (left column) and samples after grinding (central and right column). Nf-Atg was used as received. All rows refer to image of the same sample at different magnification. SEM images show typical asbestos-like morphology of Caledonian Atg.

However, Atg was markedly more resistant to dissolution than Ctl in both simulated body fluids (SBF). In acidic SBF, antigorite released 6 times less of Mg and about a half of Si with respect to chrysotile, when compared at the same mass. In neutral environment Mg_{Ctl}/Mg_{Atg} and Si_{Ctl}/Si_{Atg} ratio in solution were 3 and 2 respectively. The lower accessibility of brucitic layer in Atg, which is due to the different crystal structure of the two serpentine polymorphs (Wicks and Whittaker, 1975), explains the lower solubility of Atg with respect to Ctl.

Such difference is suggestive of a higher biopersistence of antigorite fibers if compared to chrysotile.

3.3. Surface reactivity

Surface reactivity was investigated by evaluating the presence of bio-accessible iron, and the ability to generate free radicals and to deplete antioxidant molecules (ascorbic acid and glutathione).

3.3.1. Bio-accessible iron

Bio-accessible ions are easily accessible surface ions that can participate in biological reactions or be released in a biological environment when minerals enter in contact with endogenous chelators.

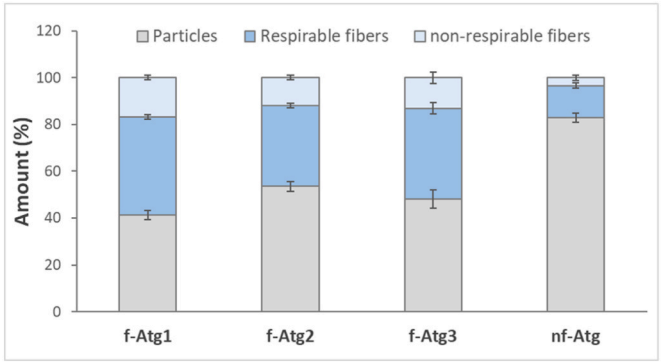

Fig. 3. *Particle and fiber distribution.* Amount of "particles" (AR <3), "respirable fibers" (AR ≥ 3, width <3 μm) and "non-respirable fibers" (AR ≥ 3, width ≥3 μm) measured by an automated image analysis system in light microscopy.

The amount of ions mobilized by iron chelators was measured both at acidic and neutral pH as a proxy of iron bio-accessibility in lysosomal fluids and in extracellular environment.

The amount of iron extracted at pH 4.5 by ferrozine in presence of ascorbic acid is reported in Fig. 6 as a function of the incubation time. Nf-Atg, f-Atg2, and f-Atg3 contained an appreciable amount of bio-accessible iron, albeit to a smaller extent than chrysotile. No iron was extracted by ferrozine alone (data not shown). After 1 week of incubation, the amount of iron removed was Ctl > f-Atg2 ≃ nf-Atg > f-Atg3 ≫ f-Atg1. Interestingly, despite the presence in the structure of a percentage of iron (about 2% of FeO) similar to that of the other samples, the amount mobilized from f-Atg1 was very small. Traces of iron were detected in solution only after a 24 h incubation and no further ions were removed after longer incubation time.

Iron may substitute for Mg in the octahedral layer and for Si in the tetrahedral layer. Most iron is located in the octahedral sheet (Mellini et al., 2002). The presence of the extended outermost octahedral layer on chrysotile accounts for the higher amount of iron released with respect to antigorite. In fact, iron release at acidic pH is promoted by Mg leaching. Accordingly, a lower amount of iron was extracted at

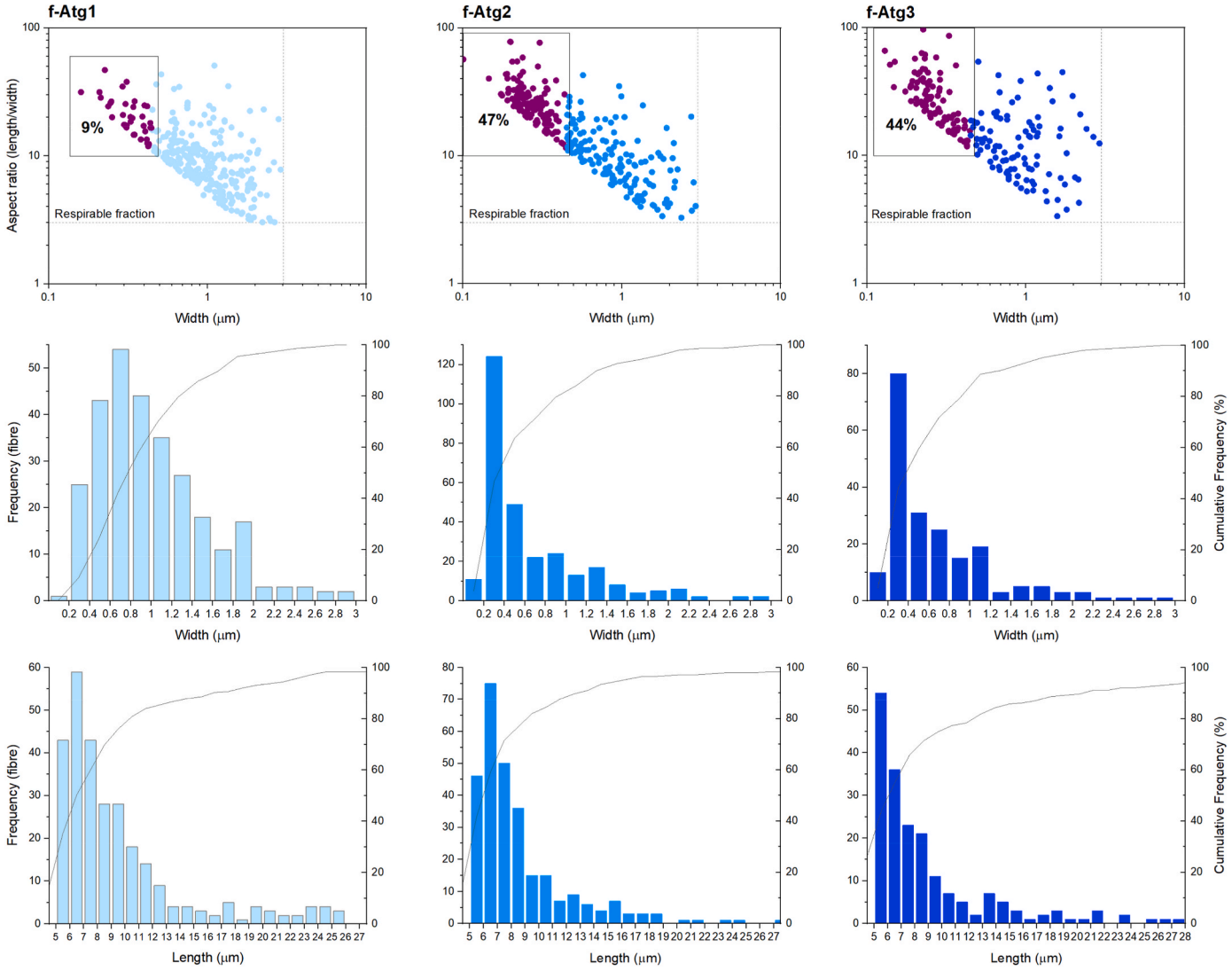

Fig. 4. *Size distribution of respirable fibers.* Scatter plots of fiber aspect ratio as a function of the fiber width (upper frame), frequency count (left axis) and cumulative frequency (right axis) of fiber width and length (bottom frames) are reported for the respirable fraction (AR ≥ 3, L > 5 μm, W < 3 μm) of milled antigorite specimens. In the scatter plots, the dimensional boundaries of "long and thin" fibers that exhibit a width <0.4 μm and an AR > 10 are highlighted (box and purple datapoints). The relative amount of these fibers is reported in the box. (For interpretation of the references to color in this figure legend, the reader is referred to the Web version of this article.)

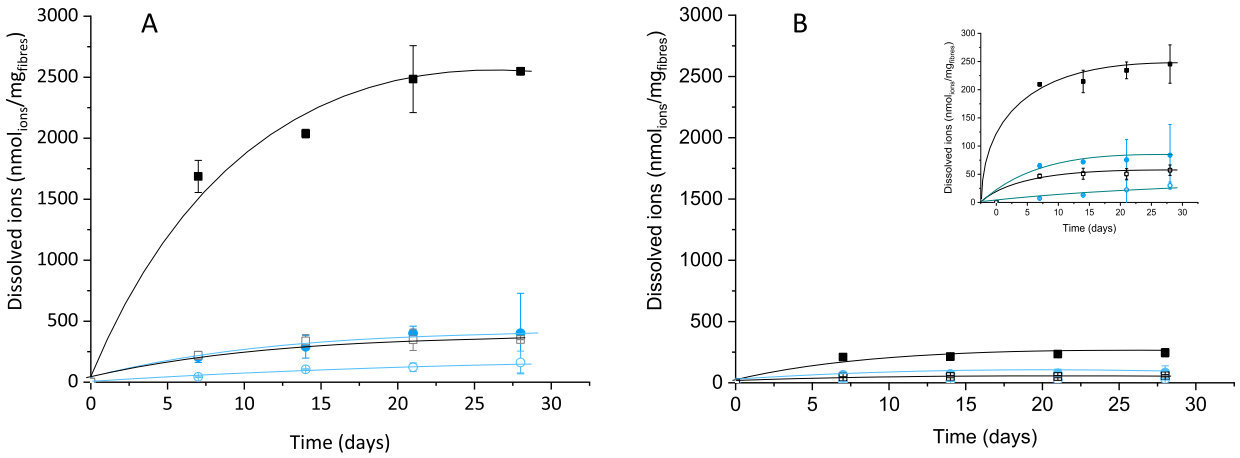

Fig. 5. ***Dissolution in simulated body fluids***. Amount of ions released in solution as a function of time (solid symbols = Mg, empty symbols = Si) by f-Atg2 (circles) and chrysotile (squares) after incubation in A) PSF and B) Gamble's solution. Inset in B: rescaled graph. The dissolution was evaluated at 37 °C, by static tests. The amount of ions released in solution was measured by ICP after 7, 14, 21, and 28 days of incubation. Experiments were performed in duplicate. Values are reported as means ± SD.

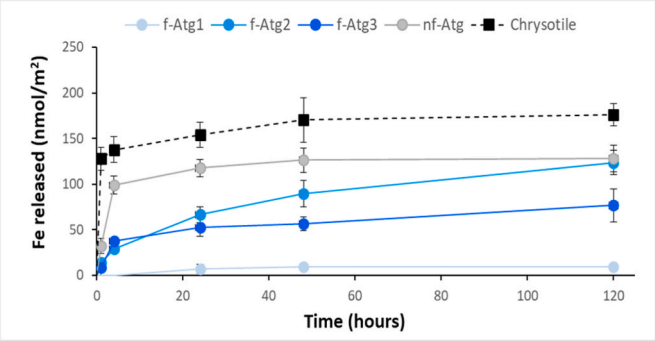

Fig. 6. *Bio-accessible iron in acidic environment.* Kinetics of Fe^{3+} release by antigorite and chrysotile at pH 4.5. The amount of iron released was measured after incubation of 1, 24, 48, and 120 h in a solution of ferrozine and ascorbic acid.

physiological pH (Fig. 4S). Also in this case, the highest amount of bio-accessible Fe was found on chrysotile.

It is worth noting that the amount of bio-accessible iron does not parallel the content of iron in the structure and was very small for all samples (0.9% for Ctl, 0.6–0.4% for f-Atg2 and f-Atg3, and 0.1% for f-Atg1).

Several molecules present in lung fluids can mobilize iron from the surface of inhaled fibers. Mobilization by endogenous chelators may induce 'iron overload' in cells after fiber phagocytosis and may contribute to the onset of cytotoxic effects. In addition, both iron poorly coordinated at the solid surface, and iron released in solution and bound to low-molecular-weight chelators is redox active and may contribute to generation of reactive oxidant species (ROS) (Gualtieri et al., 2019).

3.3.2. Free radical release

Two mechanisms of radical release were investigated:

- hydroxyl ($^{\bullet}OH$) radical release in presence of H_2O_2. This mechanism can take place in phagolysosomes of alveolar macrophages following fiber phagocytosis
- carboxyl ($CO_2^{-\bullet}$) radical release in presence of formate anion ($H–CO_2^-$), used as target molecule for mimicking a particle-induced homolytic cleavage of a C–H bond. This mechanism may take place in the presence of different molecules (lipid, peptide etc.) that contain C–H bonds.

After 1 h-incubation time of the mineral fibers in H_2O_2 solution, $^{\bullet}OH$ radical was revealed by the appearance of the typical 4-line spectrum of the [DMPO-OH]$^{\bullet}$ adduct (Fig. 7A). All antigorite specimens, except f-Atg1, catalyzed $^{\bullet}OH$ formation to a similar extent. A significant reactivity was observed also after longer incubation (1 week) in H_2O_2 (Fig. S5), suggesting the presence of catalytic reactive sites at the fiber surface. Opposite to chrysotile, antigorites did not generate carboxyl radicals (Fig. 7B) in the presence of ascorbic acid (none of the tested samples, chrysotile included, released carboxyl radicals in absence of AA, data not shown). Free radical generation is ascribed to the presence of exposed iron reactive sites, the characteristics of which are still partially unclear. Previous studies demonstrated that only poorly coordinated Fe^{2+} is responsible for $CO_2^{-\bullet}$ production, whereas both Fe^{2+}, through Fenton reaction, and Fe^{3+}, through Haber Weiss cycle, may be involved in $^{\bullet}OH$ release (Andreozzi et al., 2017; Turci et al., 2011). The absence of bio-accessible Fe^{2+} on the surface layers might explain the lack of carboxyl radical generation. However, whereas chrysotile became reactive in presence of AA, which reduces Fe^{3+} to Fe^{2+}, all antigorite samples remained inactive. Note that all samples contain Fe^{3+} ions, which can be rapidly reduced by AA (Fig. 6). The fiber reactivity, therefore, is not simply related to the presence of bio-accessible iron but also to the surface configuration in which these ions are embedded within the structure in agreement with previous studies (Andreozzi et al., 2017; Turci et al., 2017; Walter et al., 2020).

3.3.3. Interaction with ascorbic acid and glutathione

The ability of antigorite to react with endogenous molecules was tested using ascorbic acid and glutathione, two of the main endogenous antioxidants. A slight depletion of both antioxidants was observed for all antigorite samples, f-Atg1 excluded. Depletion was lower than that induced by chrysotile and no significant difference was observed among the samples (Fig. S6).

3.4. Cellular tests

Cytotoxicity, ability to induce oxidative stress, and inflammatory potential were investigated *in vitro* on human lung alveolar epithelial cells (A549) and on murine alveolar macrophages (MH-S).

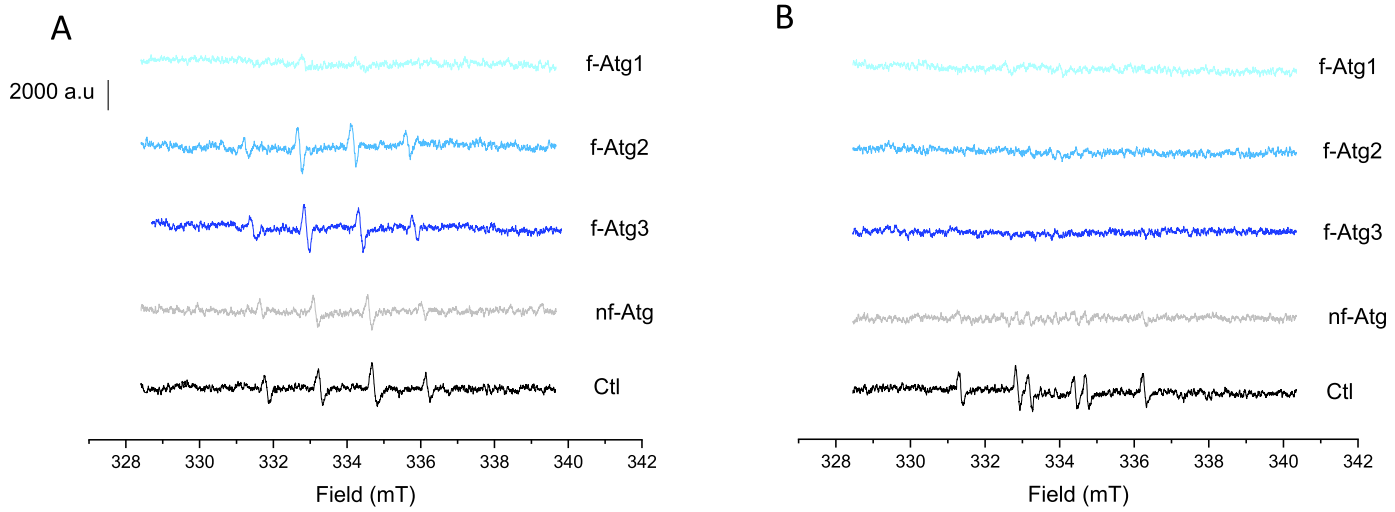

Fig. 7. *Free radical release.* EPR spectra of (A) [DMPO-OH] $^{\bullet}$ and (B) [DMPO-CO^{2-}]$^{\bullet}$ adduct recorded after 1 h of incubation of antigorite or chrysotile in a buffered solution (pH 7.4) containing H_2O_2 or HCOONa, respectively.

For oxidative stress, oxidative damage, and pro-inflammatory response we reported only data obtained with 120 μg/ml of antigorite samples, since no cellular responses were elicited at lower doses (data not shown).

3.4.1. Cytotoxicity

Cytotoxic effects were observed on both cell lines exposed to f-Atg2, f-Atg3, and chrysotile. f-Atg2 and f-Atg3 induced dose-dependent response with comparable effect on A549 (Fig. 8 A), but f-Atg3 was more cytotoxic than f-Atg2 on MH-S. A significant increase in release of lactate dehydrogenase (LDH) was observed in MH-S incubated with 30 μg/ml of f-Atg3, whereas f-Atg2 induced only weak cytotoxicity at the highest dose (Fig. 8 B). Both samples were less cytotoxic than chrysotile. No LDH release was detected in presence of f-Atg1 or non-fibrous sample on both cell lines.

3.4.2. Oxidative stress

Oxidative stress is a state of imbalance between the production of pro-oxidant reactive species and antioxidant defenses in favor of the former. This imbalance can lead to irreversible cell damage.

The ability of antigorite to induce oxidative stress was assessed by measuring a) generation of reactive oxygen species (ROS), b) decrease of the intracellular concentration of reduced glutathione (GSH); c) inactivation of the pentose phosphate pathway, and d) expression of heme oxygenase 1 (HO-1).

An increase in intracellular level of ROS was observed in A549 after incubation with f-Atg2 and in MH-S after incubation with f-Atg3 (Fig. 9A).

A weak although not significant increase of ROS was observed also in macrophages exposed to f-Atg2. No ROS generation was elicited by f-Atg1 and nf-Atg.

F-Atg2 and f-Atg3 caused a reduction of the intracellular level of GSH, both in epithelial and in macrophages cells (Fig. 9B). The effect elicited by 120 μg/ml of the antigorite samples was comparable to that induced by 30 μg/ml chrysotile. Similarly to what was observed for ROS generation, f-Atg1 and nf-Atg did not affect the intracellular level of GSH.

Fig. 9C shows the effect of antigorite on the activity of glucose-6-phosphate dehydrogenase (G6PD). G6PD is the first enzyme in the pentose pathway phosphate (PPP) cycle of which it is the limiting step and whose speed it controls. PPP is the primary route by which the cell regenerates GSH from oxidized glutathione. As previously described for crocidolite (Riganti et al., 2002), amosite (Riganti et al., 2003), and chrysotile itself (Gazzano et al., 2005), asbestos fibers inhibit PPP by affecting the activity of G6PD. In agreement, G6PD activity decreased after incubation of cells with chrysotile, whereas incubation with

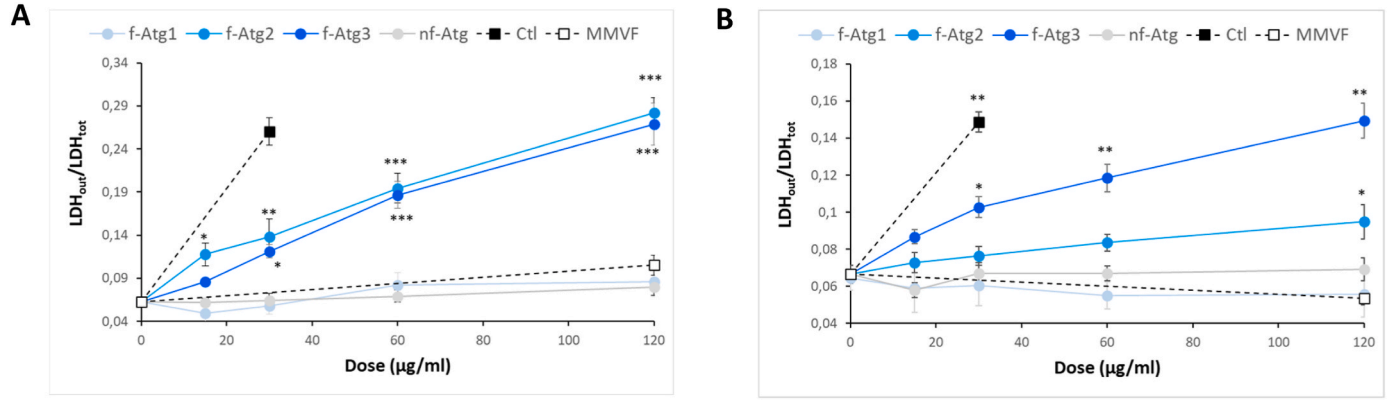

Fig. 8. Cytotoxicity: amount of LDH detected in the culture medium of (A) alveolar epithelial cells (A549) and (B) alveolar macrophages (MH-S) after incubation with f-Atg1, f-Atg2, f-Atg3, and nf-Atg at 15, 30, 60, and 120 μg/ml. UICC chrysotile (30 μg/ml) and glass fibers (MMVF10, 120 μg/ml) were used as positive and negative control, respectively. Measurements were performed in duplicate and data are presented as average ± SEM (n = 3). Asterisk indicates significant difference between cells treated with sample and control cells (CTRL): *p < 0.05, **p < 0.003, ***p < 0.0001.

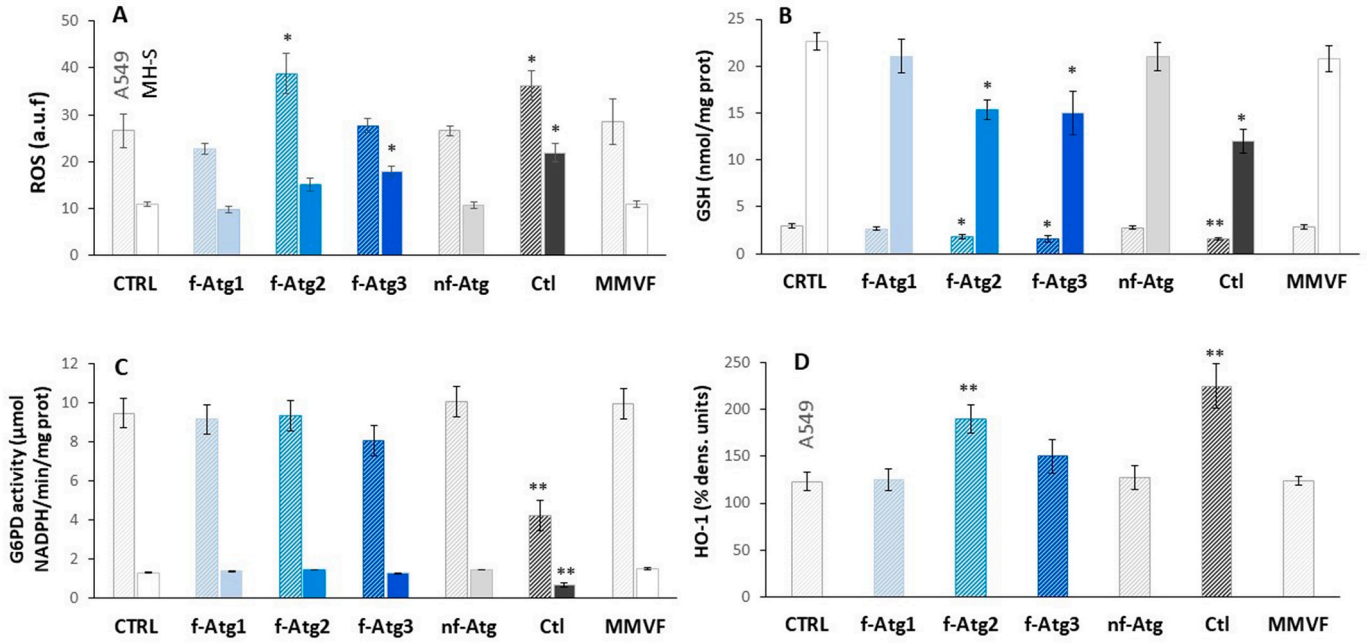

Fig. 9. Oxidative stress induced on alveolar epithelial cells (A549, dashed bars) and alveolar macrophages (MH-S, full bars) by antigorite (120 µg/ml), chrysotile (30 µg/ml), and glass fibers (MMVF, 120 µg/ml). A) ROS generation, B) reduction of intracellular level of GSH, C) inactivation of the pentose phosphate pathway, and D) expression of heme oxygenase 1 (HO-1). ROS were measured by means of a fluorescent probe (DCFH-DA). GSH levels were measured by a spectrophotometric method. Inactivation of the pentose phosphate pathway was evaluated by measuring G6PD activity. The intracellular content of HO-1 was assessed by Western Blot, using specific antibodies. All measurements were performed in duplicate and data are presented as means ± SEM (n = 3). Asterisk indicates significant difference between sample and control (Ctrl, non-exposed cells): *p < 0.05, **p < 0.01.

antigorite fibers, regardless of sample, had no effect.

Finally, Fig. 9D displays the effect of antigorite on expression of heme oxygenase 1 (HO-1) in A549 cells. HO is an enzyme system involved in the heme catabolism and HO-1 is the isoform induced in response to stimuli that cause a change in the cell redox state. A significant increase in the expression of HO-1 was observed after cellular exposure to f-Atg2 and chrysotile. A slight, but not significant, increase was observed also in cells treated with f-Atg3, while cells incubated with f-Atg1 or nf-Atg showed no increase.

3.4.3. *Oxidative damage*

Oxidative damage (Fig. 10) was evaluated by measuring a degradation product (malondialdehyde, MDA) of cell membrane lipids and DNA damage by comet assay.

MDA levels in A549 cells were increased after exposure to f-Atg2, f-Atg3, and chrysotile, but not after exposure to f-Atg1 or nf-Atg, nor in MH-S.

A significant DNA damage was induced on A549 by f-Atg2, f-Atg3, and Ctl as revealed by comet images that show a large, dispersed tail. Image analysis confirmed a significant increase in tail length, percentage of DNA in tail, and tail moment of comets. Percent of fragmented DNA in the tails was about 15% after exposure to 60 µg/ml of f-Atg2, f-Atg3 and did not significantly differ from percent of tail observed following exposure to 30 µg/ml chrysotile fibers.

3.4.4. *Inflammatory effects*

Pro-inflammatory activity of antigorite has been evaluated by measuring the production of nitric oxide (NO) and cytokine tumor necrosis factor α (TNF-α).

NO is an intracellular cytotoxic and pro-inflammatory messenger, synthesized by a family of enzymes called NO synthases. TNF-α (Tumor Necrosis Factor) is part of a group of cytokines involved in systemic inflammation and in the acute reaction phase.

F-Atg1 and nf-Atg did not stimulate the cellular production of NO. Conversely, f-Atg2 and f-Atg3 induced a significant increase in NO intracellular level on both A549 and MH-S cells. The response was similar to that observed in cells exposed to 30 µg/ml of chrysotile (Fig. 11A).

TNF-α was released in MH-S cells exposed to 120 µg/ml of f-Atg3 or 30 µg/ml chrysotile (Fig. 11B). The TNF-α levels were about 10 times higher in treated cells than in untreatred cells.

Fig. 12 allows the simultaneous visualization of the cellular effects induced by antigorite and chrysotile on the two cell lines. Overall, several cellular effects elicited by chrysotile are triggered also by two of the tested fibrous antigorite specimens, namely f-Atg2 and f-Atg3. Some cellular responses (NO generation and GSH depletion) were induced at similar extent by both fibrous specimens. Other effects (e.g., cytotoxicity) were elicited with different intensity depending on the cell line. Alveolar epithelial cells were more sensitive to antigorite than macrophages. f-Atg2 induced LDH release, oxidative stress (ROS generation, GSH depletion, HO-1 expression), oxidative damage (lipoperoxidation and DNA damage), and NO release in A549, but not ROS generation and lipid peroxidation in MH-S. f-Atg3 induced similar effect of f-Atg2 in A549 (except for a lower oxidative stress with no ROS generation and HO-1 activation) but induced only weak cytotoxicity and no lipoperoxidation in MH-S. Lower sensitivity of macrophages towards oxidative stress and oxidative damage with respect to other cell types was observed also by Cardile and colleagues (Cardile et al., 2007).

The non-fibrous sample (nf-Atg), despite the significant surface reactivity and the high presence of bio-accessible iron, was not able to induce adverse cellular responses. These results are in agreement with previous studies on prismatic antigorite that did not reveal adverse effects on cultured cells, except a weak cytotoxicity (Mossman, 2008). Similarly, studies conducted over the last 30 years on amphiboles (Ilgren, 2004), shows that riebeckite and grunerite, the non-asbestiform analogues of crocidolite and amosite, are non-toxic (Addison and McConnell, 2008; Gamble and Gibbs, 2008; Ilgren, 2004). A recent study comparing asbestiform (AR = 17) to non-asbestiform tremolite and crocidolite (AR = 5) showed that both amphiboles induce LDH leakage in AM, but the asbestiform samples are the most active in

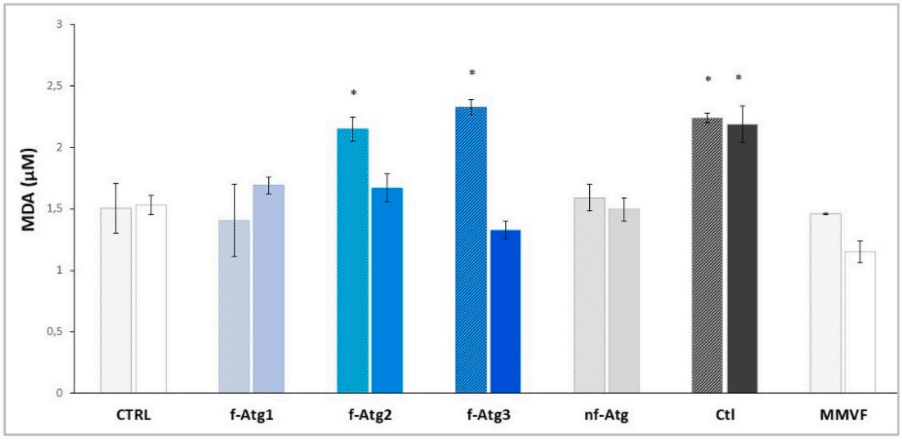

	Control	f-Atg1	f-Atg2	f-Atg3	nf-Atg	Ctl	MMVF
Comet images	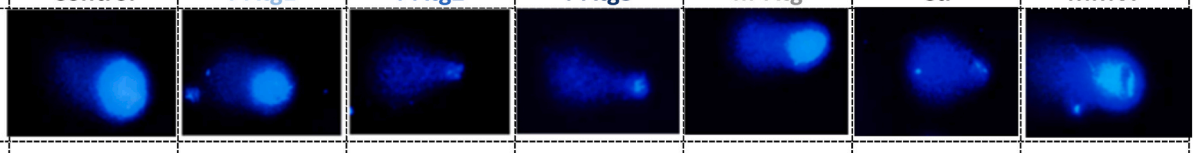						
Tail length (µm)	13.0 ± 0.8	15.2 ± 0.9	89.0 ± 2.2*	63.0 ± 2.4*	19.5 ± 1.3	102.5 ± 3.2**	14.7 ±1.2
Tail DNA (%)	1.6 ± 0.3	1.9 ± 0.2	15.6 ± 1.0*	14.9 ± 2.0*	1.8 ± 0.2	18.0 ± 3.0**	1.5 ±0.2
Tail moment (%)	0.31 ± 0.0	0.41 ± 0.1	3.2 ± 0.5*	3.1 ± 0.5*	0.5 ± 0.1	4.5 ±0.2**	0.6 ± 0.1

Fig. 10. Oxidative damage. (Upper) lipoperoxidation induced on alveolar epithelial cells (A549, dashed bars) and alveolar macrophages (MH-S, full bars) by antigorite (120 µg/ml), chrysotile (30 µg/ml), and glass fibers (MMVF, 120 µg/ml). MDA levels were measured by a spectrophotometric method. All measurements were performed in duplicate and data are presented as means ± SEM (n = 3). Asterisk indicates significant difference between sample and control (Ctrl, non-exposed cells): *p < 0.05. (Bottom) representative images of DNA comets obtained after 24 h of incubation without (control) or with antigorite (f-Atg1, f-Atg2, and f-Atg3, 60 µg/ml), chrysotile (30 µg/ml), and glass fibers (MMVF, 120 µg/ml) and image analysis parameters: tail length (distance between the center of the comet head and the last non-zero pixel of the comet profile); tail DNA (% of DNA in the tail); tail moment (product of the tail length and the percentage of total DNA in the tail).

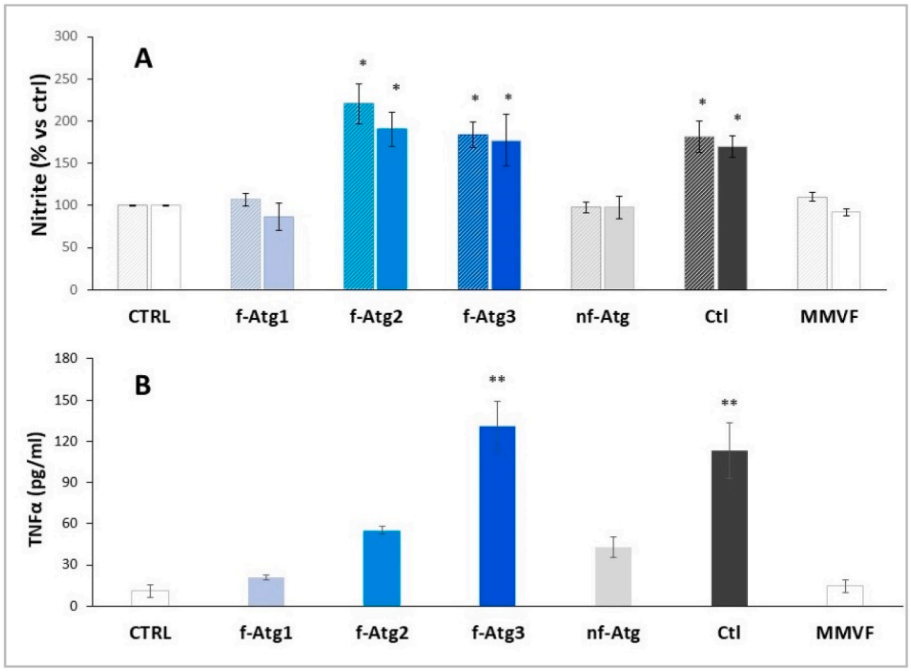

Fig. 11. Pro-inflammatory effects induced on alveolar epithelial cells (A549, dashed bars) and alveolar macrophages (MH-S, full bars) by antigorite (120 µg/ml), chrysotile (30 µg/ml), and glass fibers (MMVF, 120 µg/ml). Amount of (A) NO and (B) TNF-α generated after 24 h of incubation. The synthesis of nitric oxide was evaluated by an indirect colorimetric method based on measurement of the amount of nitrite, a stable derivative of NO. The levels of TNF-α were evaluated by ELISA assay. Measurements were performed in duplicate and data are presented as an average ± SEM (n = 3). Asterisks indicate means significantly different from the control (non-incubated cells):*p < 0.05.

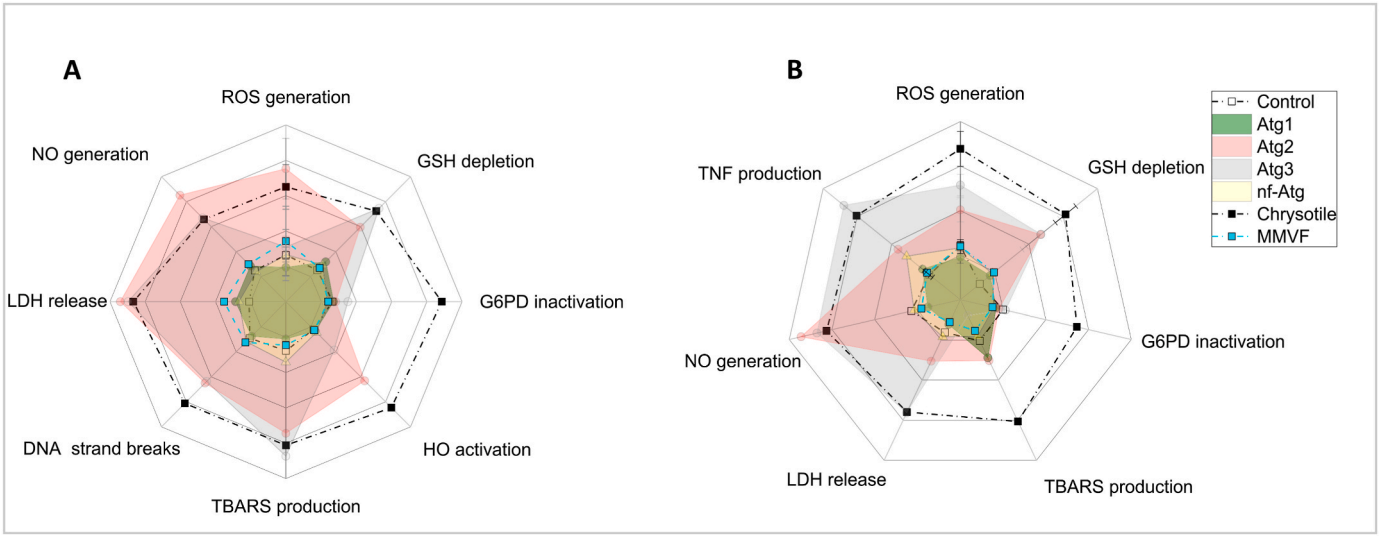

Fig. 12. Comparison of the cellular effects induced by antigorite (120 μg/ml), chrysotile (30 μg/ml), and glass fibers (MMVF, 120 μg/ml) on A) alveolar epithelial cells (A549) and B) alveolar macrophages (MH-S).

dysregulating a number of genes responsible for acute inflammation (Khaliullin et al., 2020). In agreement, Cardile and colleagues showed that asbestiform antigorite (14–20 μm long and from 0.08 to 0.4 μm wide) is cytotoxic, generates ROS and NO, and induce lipid peroxidation in macrophages and mesothelial cells (Cardile et al., 2007). Note that these studies highlighted the role of fibrous shape in *vitro* toxicity, but did not provide information about the surface reactivity of the samples.

The adverse cellular responses were induced by fibrous Caledonian samples at lower extent with respect to chrysotile. The dose of antigorite used in cellular tests was four times higher (120 μg/ml) than that of chrysotile (30 μg/ml), if compared per mass, and 3–5 times higher when compared per surface area (f-Atg2 = 14.5 cm^2/ml; f-Atg3 = 24 cm^2/ml and chrysotile 4.7 cm^2/ml). Cardile observed adverse effects already at low doses (5 μg/ml). This could be due to the asbestiform habit of the sample, with very thin and long fibers, which are considered the most pathogenic ones. f-Atg2 and f-Atg3 contained 15% and 17% of fibers with AR>20 and 11 and 14% of fibers with 10 < AR<20 respectively, but they contained also a substantial amount of other EMPs whose contribute to the onset of toxic effects is yet unclear.

Note that, although the cellular effects were lower than those induced by chrysotile, the dissolution rate in simulated body fluids of antigorite was slower and this may results in a higher biopersistence.

Interestingly, similarly to nf-Atg, f- Atg1 did not induce cellular effects. f-Atg1 length distribution matches those of the two cytotoxic fibrous antigorites. This sample contain about 60% of EMPs and more than 40% of respirable fibers following WHO definition, most part of which (58%) with width less than 1 μm. On a morphological point of view, f-Atg1 differs from f-Atg2 and f-Atg3 in the smaller amount of thin and high aspect ratio fibers (width<0.4 μm and AR > 10) that account for 9% of the respirable fraction, corresponding to 4% of the whole sample. The amount of those fibers in f-Atg2 and f-Atg3 was 47% and 44% of the respirable fraction (16 and 17% of the whole sample) respectively. Further, f-Atg1 was not able to catalyze free radical generation, to oxidize antioxidant molecules and to release iron ions. This suggests that both high surface reactivity and fibrous morphology are required to induce cellular toxicity, and that high surface reactivity and fibrous shape are necessary but not sufficient conditions to observe these effects. High surface reactivity may promote unbalance of cellular redox status. Depletion of antioxidant molecules and production of oxidant species due to the surface reactivity combine with the same effects due to frustrated phagocytosis, leading to a severe oxidative stress (IARC, 2012; Kamp and Weitzman, 1999; Liu et al., 2013). Oxidative stress, in turn, causes oxidative damage to biological macromolecules, DNA included, and activates inflammatory process.

The negligible surface reactivity observed for f-Atg1, opposite to f-Atg2 and f-Atg3, was likely due to the lower chemical alteration induced by supergene processes, which causes redistribution of the leached elements, possibly affecting iron bioavailability and promoting surface erosion. The alteration of the surface layers could lead to an increase of poorly coordinated redox active ions, which can increase the oxidizing properties of the surface. However, as this is the first work examining the reactivity of chemically altered antigorite, further studies are needed to confirm the role of supergene process in determining both chemical reactivity and cellular toxicity.

In this work we limited our consideration to the comparative assessment of three chemically and morphologically different Atg specimens from New Caledonia. As the number of fibrous particles in the chrysotile sample is expected to be higher than in f-Atg samples, cellular data should not be directly compared and chrysotile was included as positive reference sample. Moreover, the work was not designed to address the complex role of cleavage fragments that might have a role in both *in chemico* and *in vitro* activity of the minerals. Similarly, this work could not completely discriminate between the effect of morphology and fiber surface chemistry.

4. Conclusion

This study highlights the high variability of the antigorite toxicity depending upon shape, mineral chemistry, and surface reactivity.

Caledonian antigorite is able to elicit adverse cellular effects when in fibrous form, with asbestos-like morphology, and when simultaneously exhibits a relevant surface reactivity. Chemically altered fibrous antigorite, containing bio-accessible iron and with surface oxidizing properties, induces oxidative stress, oxidative damage, and pro-inflammatory response in cultured cells. Conversely, less chemically altered fibrous antigorite with low surface reactivity and low content of asbestos-like fibers, and non-fibrous antigorite are non-toxic in macrophages and alveolar epithelial cells.

Due to the slow dissolution kinetics, antigorite fibers could be more biopersistent than chrysotile.

Further studies are needed to verify the role of chemical alteration in modulating surface reactivity and cell toxicity.

Declaration of competing interest

The authors declare that they have no known competing financial interests or personal relationships that could have appeared to influence the work reported in this paper.

Data availability

Data will be made available on request.

Acknowledgements

This study is a part of a multidisciplinary project “Amiante et Bonne Pratiques (ABP) » supported by the Center National de Recherche Technologique (CNRT- Nouméa, Nouvelle Calédonie).

JRP post-doc position is funded by the University of Torino (CHI. 2019.08/XXI “Development of innovative tools for the risk assessment of elongated mineral particles (EMP) in natural environment”) and by the INAIL - BRIC 2019 project (grant number ID 57.1).

Appendix A. Supplementary data

Supplementary data to this article can be found online at https://doi.org/10.1016/j.envres.2022.115046.

References

Addison, J., McConnell, E.E., 2008. A review of carcinogenicity studies of asbestos and non-asbestos tremolite and other amphiboles. Regul. Toxicol. Pharmacol. 52, S187–S199.
Andreozzi Pacella, A., G., Corazzari, I., Tomatis, M., Turci, F., 2017. Surface reactivity of amphibole asbestos: a comparison between crocidolite and tremolite. Sci. Rep. 7, 1-9.
ANSES, 2014. Evaluation de la toxicité de l’antigorite". Avis d’expert, Saisine n° 2012-SA-0199, Agence nationale de sécurité sanitaire de l’alimentation, de l’environnement et du travail. Maisons-Alfort, France.
Barlow, C.A., et al., 2017. Asbestos fiber length and its relation to disease risk. Inhal. Toxicol. 29, 541–554.
Baumann, F., et al., 2011. Pleural mesothelioma in New Caledonia: associations with environmental risk factors. Environ. Health Perspect. 119, 695–700.
Baur, X., 2018. Review on the adverse health effects of asbestiform antigorite, a non-regulated asbestiform serpentine mineral. Am. J. Ind. Med. 61, 625–630.
Belluso, E., et al., 2020. Naturally occurring asbestiform minerals in Italian western Alps and in other Italian sites. Environ. Eng. Geosci. 26, 39–46.
Berman, D., Crump, K., 2003. Technical support document for a protocol to assess asbestos-related risk. Washington, DC, 20460.
Berman, D.W., Crump, K.S., 2008. A meta-analysis of asbestos-related cancer risk that addresses fiber size and mineral type. Crit. Rev. Toxicol. 38, 49–73.
Boulanger, G., et al., 2014. Quantification of short and long asbestos fibers to assess asbestos exposure: a review of fiber size toxicity. Environ. Health 13, 1.
Carbone, M., et al., 2011. Erionite exposure in North Dakota and Turkish villages with mesothelioma. Proc. Natl. Acad. Sci. U. S. A 108, 13618–13623.
Cardile, V., et al., 2007. Toxicity and carcinogenicity mechanisms of fibrous antigorite. Int. J. Environ. Res. Publ. Health 4, 1–9.
Deer, W.A., et al., 2009. Rock Forming Minerals: Layered Silicates Excluding Micas and Clay Minerals, Volume 3B. Geological Society of London.
EPA, 2014. Toxicological review of Libby amphibole asbestos. Integrated Risk Information System. National Center for Environmental Assessment. Environmental Protection Agency, Washington DC.
FitzGerald, J.D., et al., 2010. Antigorite from rowland flat, south Australia: asbestiform character. Eur. J. Mineral 22, 525–533.
Gamble, J.F., Gibbs, G.W., 2008. An evaluation of the risks of lung cancer and mesothelioma from exposure to amphibole cleavage fragments. Regul. Toxicol. Pharmacol. 52, S154–S186.
Gazzano, E., et al., 2005. Different cellular responses evoked by natural and stoichiometric synthetic chrysotile asbestos. Toxicol. Appl. Pharmacol. 206, 356–364.
Gerard-Monnier, D., et al., 1998. Reactions of 1-methyl-2-phenylindole with malondialdehyde and 4-hydroxyalkenals. Analytical applications to a colorimetric assay of lipid peroxidation. Chem. Res. Toxicol. 11, 1176–1183.
Ghigo, D., et al., 1998. Chloroquine stimulates nitric oxide synthesis in murine, porcine, and human endothelial cells. J. Clin. Invest. 102, 595–605.
Gianfagna, A., et al., 2003. Characterization of amphibole fibres linked to mesothelioma in the area of Biancavilla, Eastern Sicily, Italy. Mineral. Mag. 67, 1221–1229.
Groppo, C., Compagnoni, R., 2007. Ubiquitous fibrous antigorite veins from the lanzo ultramafic massif, internal western Alps (Italy): characterisation and genetic conditions. Period. Mineral. 76, 169–181.
Groppo, C., et al., 2006. Micro-Raman spectroscopy for a quick and reliable identification of serpentine minerals from ultramarics. Eur. J. Mineral 18, 319–329.
Gualtieri, A.F., et al., 2019. Iron from a geochemical viewpoint. Understanding toxicity/pathogenicity mechanisms in iron-bearing minerals with a special attention to mineral fibers. Free Radic. Biol. Med. 133, 21–37.
Harper, M., 2008. 10th anniversary critical review: naturally occurring asbestos. J. Environ. Monit. 10, 1394–1408.
Harper, M., et al., 2008. Differentiating non-asbestiform amphibole and amphibole asbestos by size characteristics. J. Occup. Environ. Hyg. 5, 761–770.
IARC, 2012. Asbestos (Chrysotile, Amosite, Crocidolite, Tremolite, Actinolite and Anthophyllite). Arsenic, metals, fibres, and dusts. World Health Organization (WHO), Lyon (F), pp. 219–309.
Ilgren, E.B., 2004. The biology of cleavage fragments: a brief synthesis and analysis of current knowledge. Indoor Built Environ. 13, 343–356.
Kamp, D.W., Weitzman, S.A., 1999. The molecular basis of asbestos induced lung injury. Thorax 54, 638–652.
Khaliullin, T.O., et al., 2020. Differential responses of murine alveolar macrophages to elongate mineral particles of asbestiform and non-asbestiform varieties: cytotoxicity, cytokine secretion and transcriptional changes. Toxicol. Appl. Pharmacol. 409.
Korchevskiy, A.A., Wylie, A.G., 2022. Dimensional characteristics of the major types of amphibole mineral particles and the implications for carcinogenic risk assessment. Inhal. Toxicol. 34, 24–38.
Liu, G., et al., 2013. Molecular basis of asbestos-induced lung disease. Annu. Rev. Pathol. 8, 161–187.
Marsh, J.P., Mossman, B.T., 1988. Mechanisms of induction of ornithine decarboxylase activity in tracheal epithelial cells by asbestiform minerals. Cancer Res. 48, 709–714.
Mellini, M., et al., 2002. Insights into the antigorite structure from Mossbauer and FTIR spectroscopies. Eur. J. Mineral 14, 97–104.
Mossman, B.T., 2008. Assessment of the pathogenic potential of asbestiform vs. non-asbestiform particulates (cleavage fragments) in in vitro (cell or organ culture) models and bioassays. Regul. Toxicol. Pharmacol. 52, S200–S203.
Mossman, B.T., Sesko, A.M., 1990. In vitro assays to predict the pathogenicity of mineral fibers. Toxicology 60, 53–61.
Petriglieri, J.R., et al., 2021. Morphological and chemical properties of fibrous antigorite from lateritic deposit of New Caledonia in view of hazard assessment. Science of the Total Environment, p. 777.
Petriglieri, J.R., et al., 2020. Identification and preliminary toxicological assessment of a non-regulated mineral fiber: fibrous antigorite from New Caledonia. Environ. Eng. Geosci. 26, 89–97.
Polimeni, M., et al., 2008. Quartz inhibits glucose 6-phosphate dehydrogenase in murine alveolar macrophages. Chem. Res. Toxicol. 21, 888–894.
Pugnaloni, A., et al., 2010. Effects of asbestiform antigorite on human alveolar epithelial A549 cells: a morphological and immunohistochemical study. Acta Histochem. 112, 133–146.
Riganti, C., et al., 2002. Crocidolite asbestos inhibits pentose phosphate oxidative pathway and glucose 6-phosphate dehydrogenase activity in human lung epithelial cells. Free Radic. Biol. Med. 32, 938–949.
Riganti, C., et al., 2003. Long and short fiber amosite asbestos alters at a different extent the redox metabolism in human lung epithelial cells. Toxicol. Appl. Pharmacol. 193, 106–115.
Scholze, H., Conradt, R., 1987. An invitro study of the chemical durability of siliceous fibers. Ann. Occup. Hyg. 31, 683–692.
Sesko, A.M., Mossman, B.T., 1989. Sensitivity of hamster tracheal epithelial cells to asbestiform minerals modulated by serum and by transforming growth factor beta 1. Cancer Res. 49, 2743–2749.
Singh, N.P., et al., 1988. A simple technique for quantitation of low-levels of DNA damage in individual cells. Exp. Cell Res. 175, 184–191.
Stanton, M.F., et al., 1981. Relation of particle dimension to carcinogenicity in amphibole asbestoses and other fibrous minerals. J. Natl. Cancer Inst. 67, 965–975.
Stefaniak, A.B., et al., 2005. Characterization of phagolysosomal simulant fluid for study of beryllium aerosol particle dissolution. Toxicol. Vitro 19, 123–134.
Tarling, M.S., et al., 2018. Distinguishing the Raman spectrum of polygonal serpentine. J. Raman Spectrosc. 49, 1978–1984.
Turci Tomatis, M., F., Lesci, I.G., Roveri, N., Fubini, B., 2011. The iron-related molecular toxicity mechanism of synthetic asbestos nanofibres: a model study for high-aspect-ratio nanoparticles. Chem.–Eur. J. 17, 350–358.
Turci, F., Tomatis, M., Pacella, A., 2017. Surface and bulk properties of mineral fibres relevant to toxicity. In: Gualtieri, A.F. (Ed.), Mineral Fibres: Crystal Chemistry, Chemical-Physical Properties, Biological Interaction and Toxicity. European Mineralogical Union, Ireland, pp. 171–214.
Utembe, W., et al., 2015. Dissolution and biodurability: important parameters needed for risk assessment of nanomaterials. Part. Fibre Toxicol. 12, 11.
Vandeputte, C., et al., 1994. A microtiter plate assay for total glutathione and glutathione disulfide contents in cultured/isolated cells - performance study of a New miniaturized protocol. Cell Biol. Toxicol. 10, 415–421.
Vortisch, W., Baur, X., 2018. Asbestiform Antigorite: a dangerous mineral in Serpentinites. A plea to treat asbestiform antigorite as an asbestos group mineral in terms of its occupational health safety effects. Neues Jahrbuch Fur Mineralogie-Abhandlungen 195, 41–64.
Walter, M., et al., 2020. Identifying the reactive sites of hydrogen peroxide decomposition and hydroxyl radical formation on chrysotile asbestos surfaces. Part. Fibre Toxicol. 17, 1–15.
Whitehouse, A.C., et al., 2008. Environmental exposure to Libby asbestos and mesotheliomas. Am. J. Ind. Med. 51, 877–880.
Wicks, F.J., O’Hanley, D.S., 1988. Serpentine minerals: structures and petrology. Hydrous phyllosilicates. De Gruyter, pp. 91–168.

Wicks, F.J., Whittaker, E., 1975. A reappraisal of the structures of the serpentine minerals. Can. Mineral. 13, 227–243.
Woodworth, C.D., et al., 1983. Induction of squamous metaplasia in organ cultures of hamster trachea by naturally occurring and synthetic fibers. Cancer Res. 43, 4906–4912.
Wozniak, H., 1984. Polish asbestos and its fibrogenic effect. I. Fibrous minerals in nickel ore deposits. Med. Pr. (Poland). 6.
Wozniak, H., et al., 1993. Experimental carcinogenicity and mutagenicity of non-asbestos natural fibres–preliminary report. Pol. J. Occup. Med. Environ. Health 6, 55–60.
Wylie, A.G., et al., 1993. The importance of width in asbestos fiber carcinogenicity and its implications for public-policy. Am. Ind. Hyg. Assoc. J. 54, 239–252.